Contrib Mineral Petrol (2006) 152: 169–186
DOI 10.1007/s00410-006-0099-y

ORIGINAL PAPER

Takashi Yoshino · Jonathan D. Price
David A. Wark · E. Bruce Watson

Effect of faceting on pore geometry in texturally equilibrated rocks: implications for low permeability at low porosity

Received: 15 August 2005 / Accepted: 24 March 2006 / Published online: 7 June 2006

Abstract The pore geometry of texturally equilibrated rocks is controlled by the interfacial energy ratio between grain boundaries and solid–liquid boundaries. Faceting at pore walls, which is a common feature of pore networks in rocks, strongly affects the liquid distribution. We investigated the effects of faceting on the equilibrium pore geometries based on image analysis of several systems with various degrees of faceting and dihedral angles. The degree of faceting was assessed by the F value, which is the ratio of the flat interface length at the pore wall to the length of total interfacial boundary between solid and liquid. The F values tend to increase with increasing liquid volume fraction. Little-faceted systems show relatively homogeneous liquid distribution. Moderately-faceted systems with a higher dihedral angle (~55°) are characterized by development of large pores surrounded by faceted walls and complementary shrinkage of triple junction tubes, whereas strongly faceted systems with a low dihedral angle show no evidence of shrinking triple junction tubes, although most pores are surrounded by faceted pore walls. The faceted systems tend to produce more facet boundaries at the pore walls due to the difference of interfacial energies between the flat and curved surfaces. In the systems with the same degree of faceting, heterogeneity of liquid distribution tends to decrease with dihedral angle. For faceting systems, the permeability of texturally equilibrated rocks with low liquid fraction would be significantly decreased by the relative reduction of triple junction volumes or by closure of channels along grain edge due to the truncation of facet walls.

Communicated by T. L. Grove

T. Yoshino · J. D. Price · D. A. Wark · E. B. Watson
Department of Earth and Environmental Sciences,
Rensselaer Polytechnic Institute, Troy, NY 12180, USA

T. Yoshino (✉)
Institute for Study of the Earth's Interior,
Okayama University, Tottori 682-0193, Japan
E-mail: tyoshino@misasa.okayama-u.ac.jp
Tel.: +81-858-433734
Fax: +81-858-433450

Introduction

Movement of fluid or melt plays a significant role in a variety of geological processes, including planetary differentiation, magma genesis, metasomatism, seismicity and heat transport. The permeability of rocks is strongly controlled by pore geometry. Although pore geometry in relatively lower temperature region, such as shallow continental crust, varies widely from grain packing to fractures, in higher temperature regions such as the lower crust and upper mantle, liquid distribution should approach an equilibrium configuration controlled by the interfacial energy minimization of the system. Therefore, accurate knowledge of the pore geometry would allow some predictions of the physical properties of liquid-bearing rocks. In an idealized system composed of identically sized grains with isotropic interfacial energy, the dihedral angle (θ) at solid–liquid–solid triple junction is a fundamental factor in determining the connectivity of liquid and the pore morphology. It is defined by (e.g., von Bargen and Waff 1986)

$$\frac{\gamma_{ss}}{\gamma_{sl}} = 2\cos\left(\frac{\theta}{2}\right) \quad (1)$$

where γ_{ss} is the solid–solid interfacial energy per unit area and γ_{sl} is the solid–liquid interfacial energy per unit area. At low liquid volume fraction (ϕ), connectivity of the liquid phase is critically dependent upon θ. If $\theta < 60°$, liquid forms an interconnected network along the grain edge (triple junction) and corner (four-grain junction). If $\theta > 60°$, liquid forms isolated pockets at the grain corner or on the grain boundary, and a critical liquid fraction is necessary to establish connectivity (e.g., von Bargen and Waff 1986). Therefore, the interconnectivity of liquid phase has been evaluated by

measuring dihedral angles. Numerous experimental studies of the wetting behavior of geological liquids have been conducted for basaltic melts (e.g., Waff and Bulau 1979), for silicic melts (e.g., Laporte 1994), and for C–O–H fluids (e.g., Watson and Brenan 1987).

Although the idealized model is characterized by smoothly curved solid–liquid interfaces with a uniform mean curvature, equilibrium textures in silicate–liquid systems generally show extensive development of crystal faces at the pore wall, that is "faceting"; we use this term hereafter to include all apparent flat pore walls (e.g., Cooper and Kohlstedt 1982; Waff and Faul 1992; Faul et al. 1994; Cmíral et al. 1998; Laporte and Watson 1995). In at least some such systems, θ alone does not determine pore geometry. Since permeability is ultimately sensitive to pore geometry at low liquid fraction, some researchers have investigated experimentally and theoretically the effect of faceting on the equilibrium liquid distribution. Price et al. (2006) reported that the tremolite-H_2O fluid system characterized by extensive faceting and a low dihedral angle (θ = 35–42°) shows an apparent percolation threshold (ϕ_{th} = 0.04) for permeability measured using a transient pulse method. Furthermore, three-dimensional numerical models of the pore geometry consisting of only the faceting crystal–liquid interface also showed the existence of a percolation threshold (Cheadle et al. 2004).

For the olivine-basaltic melt system, the effect of the observed moderate faceting on permeability has been controversial. Based on the observation that most of the melt is located in thin and elongated inclusions on polished sections, Faul et al. (1994) suggested that melt morphology is approximated by an oblate ellipsoid in three dimensions instead of tubular network of melt-filled triple junctions along three-grain edges. Furthermore, Faul (1997) hypothesized far lower permeabilities than predicted by von Bargen and Waff (1986) at melt fractions below the threshold value (ϕ_{th} < 0.02–0.03). If melt fraction exceeds ϕ_{th}, the resulting interconnection of the disk-shaped pores produces an increase in permeability over nine orders in magnitude (Faul 2001). Wark et al. (2003), however, questioned their hypothetical model based on a more critical analysis of pore microstructure and suggested that melt occupies a triple junction network. Based on the power law relationship between grain boundary wetness and liquid volume fraction, Yoshino et al. (2005) also reported that melt geometry of partially molten peridotite can be approximated by a triple junction tube.

Many researchers who have studied pore morphology in anisotropic polycrystalline aggregates have used the term "crystal anisotropy" to explain the deviation of the pore morphology from the ideal model, which assumes uniformly curved pore walls (e.g., Waff and Faul 1992; Faul et al. 1994; Cmíral et al. 1998; Laporte and Watson 1995). For common geological systems, the most notable deviation from the constant interfacial curvature predicted by the isotropic model is the presence of flat or faceted crystal–liquid interfaces. Most flat interfaces correspond to the planar solid–liquid interfaces parallel to crystallographic planes with minimum energy; low Miller index planes. It is not always clear what is meant by "anisotropy", because by definition any crystalline material will be anisotropic with respect to surface energy. This fact alone, however, is not the necessary and sufficient condition as a cause of the deviation from the homogeneous liquid distribution predicted from the ideal model. Minerals that are strongly anisotropic with respect to interfacial energies do not always display facets, whereas those that are more isotropic with respect to interfacial energies may be strongly faceted for the same T, P, and liquid composition. Therefore, we prefer to use the term "faceting" rather than "crystal anisotropy" in the following sections.

The main purpose of this study is to elucidate the effect of faceting on permeability. Since pore morphology depends on the "degree of faceting" (F) in the system, the relationship between F and liquid distribution should be considered in predicting the permeability. First, the F value is defined by a ratio of the length of faceted pore wall to the total length of pore wall on the polished sections and were measured from several systems with various θ and liquid volume fraction (ϕ) based on image analysis of electron micrographs. To semi-quantitatively estimate the effect of faceting on liquid distribution and grain and pore size distributions (PSDs), polished sections were systematically investigated by image analysis. It is shown that development of faceting at the pore wall for texturally equilibrated rocks leads to more inhomogeneous liquid distribution than the system with little faceting. Based on the distinct difference of PSD on the polished section between faceted and little-faceted systems, we finally discuss causes of the low permeability for the faceting system at low ϕ.

Methods

Definition of degree of faceting (F)

Considering a single crystal in a very large melt or fluid reservoir, a growing single crystal surrounded by liquid tends toward shape dictated by the Gibbs–Wulff plot of surface energy versus crystallographic orientation (e.g., Herring 1951). If a flat (faceted) surface has lower energy than a surface that is curved, the faceted surface will be the stable form. For cubic crystals, the overall form of a crystal that has both curved and faceted surfaces can be represented by aspect ratio (shortest axis/longest axis) of distances between pairs of rounded segments and pairs of faceted segments (e.g., Warren 1968; Garbrisch et al. 2001). However, the analysis for a Wulff crystal is not valid for a crystal–liquid aggregate as examined by this study. Furthermore, it is difficult to assess the degree of faceting by aspect ratio for most silicate minerals. Therefore, we newly define the degree of faceting (F) as a thermodynamic expression.

The driving force for textural equilibration is surface energy minimization. The total Gibbs free energy due to solid–liquid surface areas is given by

$$\Delta G_{\mathrm{sl}} = \sum_i \bar{A}_i \bar{\gamma}_i + \sum_i \tilde{A}_i \tilde{\gamma}_i \tag{2}$$

where A is the surface area and γ is the solid–liquid interfacial energy; the over "bar" represents the faceted surface; and symbols with $\sim$ represent the curved interface. The fraction of the free energy contributed by the faceted surface (R) is given by

$$R = \frac{\Delta \bar{G}_{\mathrm{sl}}}{\Delta G_{\mathrm{sl}}} = \frac{\sum_i \bar{A}_i \bar{\gamma}_i}{\sum_i \bar{A}_i \bar{\gamma}_i + \sum_i \tilde{A}_i \tilde{\gamma}_i}. \tag{3}$$

When the mean surface tension of the flat interfaces ($\bar{\gamma}_i$) is the same as (or very close to) the mean surface free energy of the curved interfaces ($\tilde{\gamma}_i$), the non-dimensional value representing the fraction of the faceted surface area over the total surface area (F) is identical to the R value. Therefore, the F value is given by

$$F = \frac{\bar{A}}{\bar{A} + \tilde{A}}, \tag{4}$$

where A in the above expression is the total surface area of the flat or curved interface. The F value defined by Eq. 4 is measurable independently of ϕ and crystal system.

Analyzed systems

We collected digitized images of several different systems from previous studies involving equilibrated grain-scale microstructures (Watson 1999; Wark and Watson 2000; Price et al. 2006; Yoshino et al. 2005) with various ϕ, θ and F to clarify effects of faceting on permeability. The analyzed systems can be visually categorized by intensity of faceting into three groups: (1) little-faceted systems (fluorite–silicate melt system with a dihedral angle of 20°, fluorite– and calcite–H_2O systems with a dihedral angle of 66°); (2) moderate-faceted systems (olivine-basaltic melt system with a dihedral angle of 34°, quartz–H_2O system with a dihedral angle of 55°); (3) strongly faceted systems (tremolite–H_2O fluid system with a dihedral angle of 35°, clinopyroxene (ferrosalite)–H_2O system with a dihedral angle of 55°). Another analyzed system is not mono-mineralic but partially molten lherzolite consisting of olivine, orthopyroxene, clinopyroxene and spinel, which is xenolith KLB1, a fertile spinel lherzolite from Kilbourne Hole, New Mexico (Takahashi 1986). Experimental details are summarized in Table 1. Analyzed images are exactly same as the images analyzed by Yoshino et al. (2005).

Microstructure

Figure 1 shows electron images of representative microstructures for several systems with various θ, ϕ and F. Little-faceted systems are characterized by visually homogeneous pore distribution irrespective of θ (Fig. 1a, b). The fluorite–silicate melt system with low θ (20°) shows that melt contacts most of grain boundaries on the polished section, even if melt fraction is very low ($\phi \sim 0.02$) (Fig. 1a). In the fluorite– and calcite–H_2O systems with high θ (66°), the pores are located on grain boundaries and/or at triple junctions at low fluid fraction ($\phi < 0.03$) (Fig. 1b). As fluid fraction increases, triple junction pores become larger and connect to the neighboring ones (see Fig. 2a, c, e). Although calcite (trigonal–hexagonal) is crystallographically more anisotropic than fluorite (cubic), the calcite–H_2O system is no more faceted than the fluorite–H_2O system.

Pore morphology of moderately-faceted system is controlled by the dihedral angles. The olivine-basalt system with a dihedral angle of 34° shows relatively uniform liquid distribution at $\phi < \sim 0.12$ (Fig. 1c), although the pores surrounded by four or more grains are more common than that of the little-faceted system. Triple junction tubule edges extend deeper into grain boundaries with increasing melt fraction. The quartz–H_2O system with a dihedral angle of 55°, shows a development of some pores surrounded by faceted pore wall (Fig. 1d). Although the triple junction tubules are stable, the apparent area of each pore occupying the triple junction is distinctly smaller than that of the little-faceted system at the same ϕ. The inhomogeneous pore distribution is independent of ϕ (Fig. 2b, d, f). The fluid phase volumetrically partitions into the large pores. The partially molten lherzolite shows completely different pore textures from the olivine-basalt system (see Fig. 2 in Yoshino et al. 2005). Orthopyroxene, clinopyroxene and spinel are stable at lower temperature runs ($< 1{,}250$°C). Melt structures around pyroxene generally have large dihedral angles, except for those adjacent to olivine (Toramaru and Fujii 1986). This is particularly true for low melt fractions ($\phi < \sim 0.03$). Therefore, melt is largely contained at grain corners. As melt fraction increases, melt morphology becomes similar to the olivine-basalt system because of decreasing pyroxene phase modes.

The tremolite–H_2O fluid system is far more faceted than the other system considered here (Fig. 1e). Although tremolite–H_2O fluid system has a dihedral angle of 35° between curved pore walls (Price et al. 2006) similar to the olivine-basalt system (34°), the pore morphology is dramatically different between them due to a difference of the degree of faceting. As ϕ increases, tremolite grains change from rounded shape to elongated or prismatic shape, suggesting that tremolite grains with faceted faces are more likely to appear at higher ϕ. The flat face is frequently truncated by the facet of other crystals. Therefore, the intersections of a grain boundary with two solid–fluid interfaces are mostly observed as an intersection between faceted pore walls. However, the pore distibution is rather homogenous. Clinopyroxene–H_2O system shows rather similar pore distribution to the quartz–H_2O system (Fig. 1f). The apparent aspect ratio

Table 1 Summary of image analysis

Image no.	ϕ (%)	F	ψ	D_{2d} (μm)	LNPA	AR	MAR	Ref
San Carlos olivine + MORB (1,350°C, 1.0 GPa)								
FDP7a1	0.3	0.17	0.08	53	−2.21(38)	ND	0.51(7)	YTWW
FDP3a1	1.6	0.12	0.29	38	−1.90(41)	0.66(19)	0.35(13)	YTWW
FDP3a2	1.7	0.11	0.28	38	−1.75(33)	0.68(16)	0.27(9)	YTWW
FDP9-3	3.3	0.20	0.42	29	−1.14(57)	0.65(18)	0.29(17)	YTWW
FDP9-7	3.6	0.21	0.48	24	−1.26(80)	0.71(14)	0.44(46)	YTWW
FDP5a2	5.1	0.27	0.50	39	−1.71(71)	0.65(15)	0.46(26)	YTWW
FDP5a1	6.6	0.36	0.52	42	ND	ND	ND	YTWW
FDP5a4	8.2	0.31	0.53	39	ND	ND	ND	YTWW
FDP7d2	10.1	0.33	0.68	40	−0.96(77)	0.68(16)	0.23(17)	YTWW
FDP8-4	11.6	0.44	0.77	30	−0.67(87)	0.70(16)	0.24(18)	YTWW
FDP7b2	13.4	0.33	0.78	55	−1.19(80)	0.66(18)	0.19(13)	YTWW
FDP8-2	14.7	0.30	0.78	40	−0.62(84)	0.71(16)	0.23(18)	YTWW
FDP3b2	15.5	0.32	0.59	29	ND	0.69(14)	ND	YTWW
FDP3b1	20.6	0.48	0.71	31	ND	ND	ND	YTWW
FDP5c2	24.5	0.38	0.88	34	ND	ND	ND	YTWW
FDP3c1	31.1	0.41	0.87	36	ND	ND	ND	YTWW
FDP5c2	40.1	0.43	0.94	35	ND	0.68(16)	ND	YTWW
FDP7f1	46.7	0.42	0.93	38	ND	0.61(16)	ND	YTWW
KLB1								
FKLB5-3	2.4	0.17	0.28	9	−1.65(43)	0.66(16)	0.30(10)	YTWW
FKLB5-5	5.3	0.31	0.40	9	−1.60(81)	0.68(18)	0.42(34)	YTWW
FKLB5-4	10.2	0.26	0.42	11	−1.37(68)	0.66(13)	0.31(12)	YTWW
FKLB4-6	13.9	0.35	0.65	18	−1.03(97)	0.67(15)	0.28(15)	YTWW
FKLB6-9	14.4	0.34	0.56	16	−1.17(93)	0.68(15)	0.30(22)	YTWW
FKLB4-6	16.5	0.35	0.66	18	−1.10(93)	0.70(14)	0.29(20)	YTWW
FKLB4-4	17.2	0.44	0.65	18	−1.39(100)	0.75(15)	0.24(15)	YTWW
FKLB3-5	27.8	0.30	0.79	23	ND	0.76(14)	ND	YTWW
FKLB2-2	29.4	0.35	0.84	25	ND	0.74(13)	ND	YTWW
FKLB2-3	31.1	0.33	0.76	24	ND	0.73(13)	ND	YTWW
Fluorite + Silicate melt								
GSFP14B3	1.6	0.00	0.27	80	−2.24(60)	0.70(10)	0.37(19)	WW00 GSFP14
GSFP14B2	2.9	0.00	0.42	68	−2.29(64)	0.67(16)	0.42(30)	WW00 GSFP14
GSFP14B1	3.2	0.00	0.46	62	−2.01(56)	0.72(11)	0.35(22)	WW00 GSFP14
GSFP17A2	4.8	0.03	0.46	60	−2.00(69)	0.69(13)	0.33(23)	WW00 GSFP17
GSFP15-1	5.7	0.00	0.56	56	−1.66(59)	0.67(14)	0.35(28)	WW00 GSFP15
GSFP17A1	9.5	0.02	0.69	49	−1.72(72)	0.74(14)	0.25(22)	WW00 GSFP17
Fluorite + H_2O								
19afr4	0.3	0.00	0.08	51	−2.60(44)	0.62(14)	0.72(26)	W99 19a
12bfr2	0.5	0.00	0.13	65	−3.45(49)	0.63(12)	0.93(47)	W99 12b (850°C)
19bfr9	0.7	0.00	0.14	43	−2.58(60)	0.66(19)	0.80(46)	W99 19b
19cfr7	1.8	0.03	0.20	42	−2.15(46)	0.72(17)	0.67(23)	W99 19c
19dfr7	2.0	0.01	0.28	53	−2.11(56)	0.75(7)	0.45(26)	W99 19d
19dfr6	2.4	0.03	0.27	50	−2.04(57)	ND	0.41(18)	W99 19d
5afr1	3.8	0.04	0.32	23	−1.73(71)	0.72(14)	0.47(36)	W99 5a
5bfr1	4.3	0.06	0.31	21	−1.69(71)	0.72(14)	0.44(26)	W99 5b
9afr2	6.7	0.01	0.39	67	−1.37(53)	0.69(13)	0.51(29)	W99 9a
8bfr1	7.2	0.03	0.41	18	−1.35(54)	0.72(12)	0.46(18)	W99 8b
9bfr1	7.5	0.02	0.44	70	−1.37(59)	0.72(14)	0.49(25)	W99 9b
8bfr3	8.7	0.03	0.44	30	−1.39(69)	0.74(13)	0.47(29)	W99 8b
10bfr1	9.3	0.03	0.44	40	−1.47(57)	0.74(12)	0.51(28)	W99 10b
6bfr1	12.3	0.02	0.49	11	−1.00(25)	0.75(14)	0.49(28)	W99 6b
9dfr1	12.9	0.03	0.54	48	−0.75(49)	0.75(12)	0.40(21)	W99 9d
9cfr1	13.0	0.02	0.51	50	−0.99(57)	0.74(13)	0.50(26)	W99 9c
8cfr1	13.8	0.05	0.53	15	−1.11(77)	0.76(11)	0.48(25)	W99 8c
8cfr2	15.0	0.03	0.52	14	−1.03(74)	0.78(13)	0.42(20)	W99 8c
8dfr5	15.4	0.05	0.54	14	−1.17(75)	0.74(12)	0.51(25)	W99 8d
Calcite + H_2O								
8bfr6	1.5	0.02	0.17	28	−2.08(53)	0.72(10)	0.54(25)	W99 8b
8bfr5	1.8	0.03	0.21	30	−2.08(52)	0.70(12)	0.56(28)	W99 8b
8bfr8	2.3	0.01	0.21	26	−2.02(65)	0.74(13)	0.62(36)	W99 8b
8dfr9	3.0	0.05	0.27	25	−1.95(55)	0.69(17)	0.53(25)	W99 8d
6bfr4	5.4	0.04	0.33	17	−1.54(56)	0.75(11)	0.56(27)	W99 6b

Table 1 (Contd.)

Image no.	ϕ (%)	F	ψ	D_{2d} (μm)	LNPA	AR	MAR	Ref
Quartz + H_2O								
19afr2	1.6	0.18	0.16	17	−2.22(68)	0.66(17)	0.71(51)	W99 19a
19afr1	2.6	0.12	0.21	17	−2.19(78)	0.66(17)	0.45(26)	W99 19a
19bfr2	3.8	0.13	0.28	16	−2.01(80)	0.70(14)	0.50(36)	W99 19b
26bfr7	4.2	0.31	0.31	32	−2.39(66)	0.70(17)	0.54(37)	W99 26b (925°C)
12afr6	4.6	0.16	0.29	19	−1.92(76)	0.71(13)	0.60(46)	W99 12a (850°C)
19bfr3	5.9	0.16	0.28	17	−1.74(83)	0.72(13)	0.66(50)	W99 19b
22afr3	7.2	0.29	0.37	30	−1.76(83)	0.71(14)	0.47(32)	W99 22a
19cfr1	7.4	0.28	0.32	21	−2.08(106)	0.69(14)	0.53(33)	W99 19c
19cfr2	11.5	0.30	0.35	24	−1.47(104)	0.71(14)	0.55(45)	W99 19c
5afr5	12.7	0.24	0.54	20	−1.87(82)	ND	0.40(29)	W99 5a
5bfr5	17.6	0.35	0.51	9	−1.00(82)	0.70(15)	0.47(39)	W99 5b
Tremolite + H_2O								
TR3	5.3	0.35	0.42	3	−1.42(59)	0.58(19)	0.31(16)	PWWS Tr3
TR4-1	15.9	0.62	0.74	6	−0.49(18)	0.51(25)	0.21(16)	PWWS Tr4
TR4-2	21.5	0.64	0.73	5	ND	0.62(16)	ND	PWWS Tr4
TR7	30.2	0.79	0.89	7	ND	0.53(17)	ND	PWWS Tr7
Clinopyroxene + H_2O								
PF12c6	1.1	0.07	0.13	20	−2.02(63)	0.70(12)	0.52(18)	WL93 PF12c
PF13e3	2.7	0.29	0.26	24	−2.11(56)	0.70(14)	0.44(20)	WL93 PF13e
PF13d1	4.1	0.28	0.25	26	−1.58(65)	0.74(19)	0.43(16)	WL93 PF13d
PF13e1	6.4	0.26	0.30	21	−1.63(66)	0.69(14)	0.45(16)	WL93 PF13d
PF13f3	7.6	0.41	0.43	21	−1.20(68)	0.72(13)	0.26(12)	WL93 PF13f
PF13f1	9.0	0.38	0.48	25	−1.52(58)	0.67(13)	0.30(14)	WL93 PF13f
PF13f2	10.3	0.43	0.48	25	−1.39(78)	0.74(11)	0.35(18)	WL93 PF13f
PF13f4	13.1	0.43	0.51	25	−1.62(93)	0.67(15)	0.41(31)	WL93 PF13f
PF13f5	20.0	0.39	0.49	22	−1.28(94)	0.66(14)	0.40(19)	WL93 PF13f

ψ represents grain boundary wetness, defined as the ratio of solid–liquid boundary area over the total area of interphase boundaries. Grain boundary wetness is defined by $\psi = A_{sl}/(A_{sl} + A_{ss})$ where A_{sl} and A_{ss} are the solid–liquid and the solid–solid interfacial areas, respectively. LNPA represents log mean pore area normalized by the average grain size determined by the polished section. AR denotes mean aspect ratio of grains defined by a ratio of shortest axis to longest axis for each grain. MAR indicates a value analogous to the aspect ratio of pore shape defined by Faul et al. (1994). YTWW (Yoshino et al. 2005), W99 (Watson 1999), WW00 (Wark and Watson 2000), WL93 (Watson and Lupulescu 1993) and PWWS (Price et al. 2006) indicate the referrences of each run
ND Non-determined

of grains is higher than it is for tremolite but is similar to that in the other systems (Table 1). Even at low ϕ, facets are common.

Image analysis

Backscattered electron images (BEI) of polished sections were obtained for the partially molten peridotite systems (olivine-basalt system and partially molten lherzolite); secondary electron images (SEI) were obtained from the polished sections for the other systems. The BEI and SEI images consist of 2,000 × 1,538 pixels and of 1,000 × 798 pixels, respectively, with a step size of 0.06–0.3 μm depending on the grain size. The least fractured areas were selected for imaging at higher magnification.

Usage of transmitted electron microscope (TEM) is probably the best way to identify a faceted plane at the atomic scale. However, the biggest problem of TEM analysis is that the analyzed area obtained from one image is restricted, too small to measure on the degree of faceting as a function of ϕ and to compare the degree of faceting with grain and PSDs. Therefore, we used the scanning electron microscope to analyze the microstructure of run products.

The gray scale images were converted to four types of the binary images (Fig. 3): (1) images tracing the entire interphase boundary (pore wall) between crystal and liquid (Fig. 3b), (2) images tracing only flat crystal faces along the pore wall (Fig. 3c), (3) images tracing grain boundaries (Fig. 3d) and (4) images showing grain shape (Fig. 3e). For partially molten peridotites, a threshold method could not be used, because olivine and pyroxene crystals have an iron-rich rim grown from melt during quenching. Since the iron-rich rims were not present at run conditions, they were treated as melt. For partially molten lherozolite, the clinopyroxene grains commonly represent non-uniform overgrowth showing dendritic or idiomorphic textures formed during quenching. These were also treated as melt. The pores of the H_2O-bearing system observed as the epoxy- or air-filled spaces were also difficult to identify using a threshold method due to the possible presence of cracks generated during quenching. Using Adobe Illustrator, the outlines of the melt- or fluid-filled pores were carefully traced on screen to create binary images. Figure 4 shows representative binary images showing pore distribution traced from gray scale images of Fig. 1. The flat faces at the pore wall were manually traced by eye as a straight line (Fig. 5). In some cases, it was difficult to judge whether

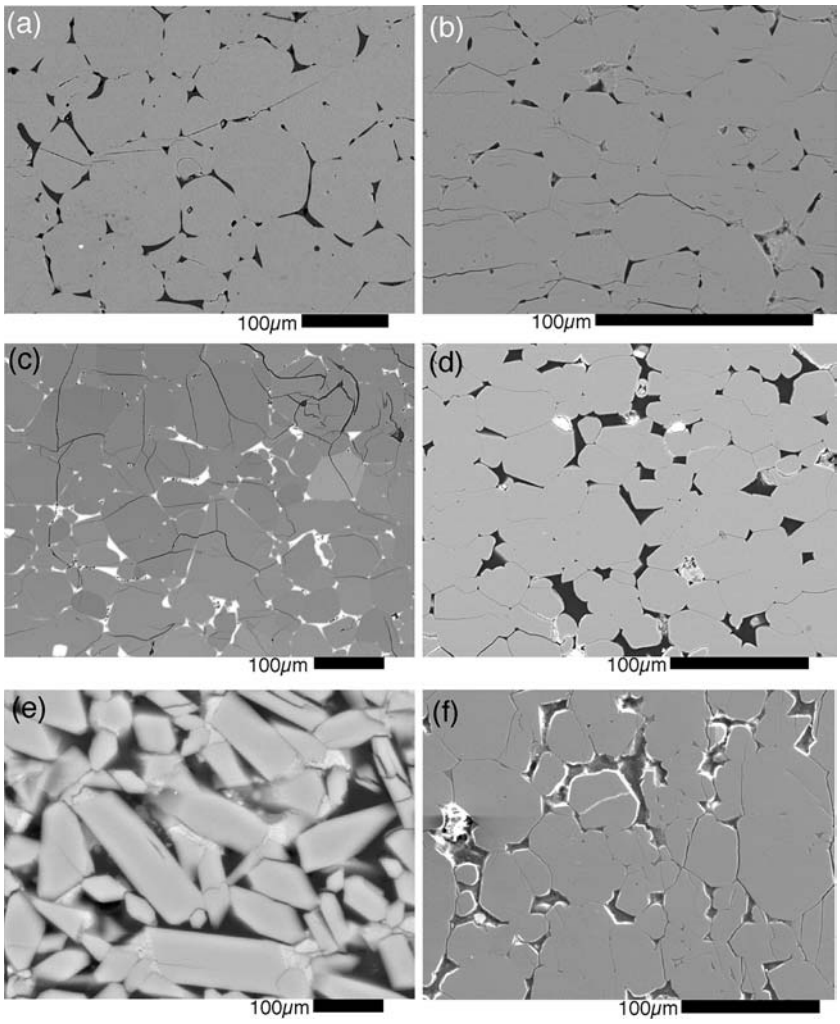

Fig. 1 Representative electron images of the polished surfaces for several systems with various dihedral angles and degrees of faceting. **a** BSE image of fluorite–K-rich silicate melt system with $\theta = 20°$ (Image No. GSFP14B2). *Darker and bright portions* correspond to the K-rich silicate melt and fluorite crystals, respectively. **b** BSE image of calcite–H_2O system with $\theta = 66°$ (Image No. 8dfr9). *Darker and bright portions* correspond to the pore and calcite crystals, respectively. **c** BSE image of olivine-basalt system with $\theta = 34°$ (Image No. FDP5a2). *Darker and bright portions* correspond to the olivine crystals and basaltic glass, respectively. **d** BSE image of quartz–H_2O system with $\theta = 55°$ (Image No. 19cfr1). *Darker and bright portions* correspond to the pore and quartz crystals, respectively. **e** SEI image of tremolite–H_2O system with $\theta = 35°$ (Image No. TR9). *Darker and bright portions* correspond to the pore and tremolite crystals, respectively. **f** SEI image of clinopyroxene (ferrosalite)–H_2O system with $\theta = 55°$ (Image No. PF13e1). *Darker and bright portions* correspond to the pore and clinopyroxene crystals, respectively

the crystal-melt interface is flat or gently curved. Therefore, the sum length of the flat face may include large errors. Grain boundaries were also traced on screen by identification of different grain orientations from high-contrast digitized images. When grain boundaries were unclear in the image, they were approximated as a straight line connecting fluid or melt pockets to each other.

Image analysis was conducted for each binary image using Image J software for Macintosh provided by NIH. The total lengths of solid–liquid boundaries (L_{sl}^{total}) and flat solid–liquid boundaries (L_{sl}^{F}) were measured to determine the degree of faceting ($F = L_{sl}^{F}/L_{sl}^{total}$). This F value is not neccessarily equal to the F value defined by Eq. 4 except for the case that the pore wall orientation is random. Because the obtained F values probably include large errors, the F values should not be evaluated as an absolute but instead as a relative value. L_{sl} was obtained as the total length of perimeter of the pores, where the intersections of the pores with the edge of the image were subtracted. Liquid volume fraction ϕ was obtained from the total area of the pores relative to the total area of each image.

To characterize the homogeneity of the pore distribution, each pore size and grain size on the polished section was also measured to determine the apparent grain and PSDs, although pores may be interconnected three dimensionally to each other when the dihedral angle is less than 60° or when ϕ is above the percolation thereshold. For systems with large ϕ, the PSDs could not be determined because the amount of measurable pore is extremely small due to the interconnection of pores on polished sections. In order to compare grain and PSDs between samples with different grain sizes, all measured data for each sample of material were normalized by the average grain size. The pore and grain sizes were estimated from the area of each pore and grain, assuming that their irregular boundary outlines could be approximated by a circle.

The analyzed areas contain over 50 grains except for some images of materials with low ϕ. For the quartz–H_2O system characterized by inhomogeneous fluid distribution, images containing over 100 grains were analyzed to avoid the effect of local fluid distribution on F, ψ (grain boundary wetness, see footnote of Table 1) and ϕ. Since the presence of secondary phase inhibits

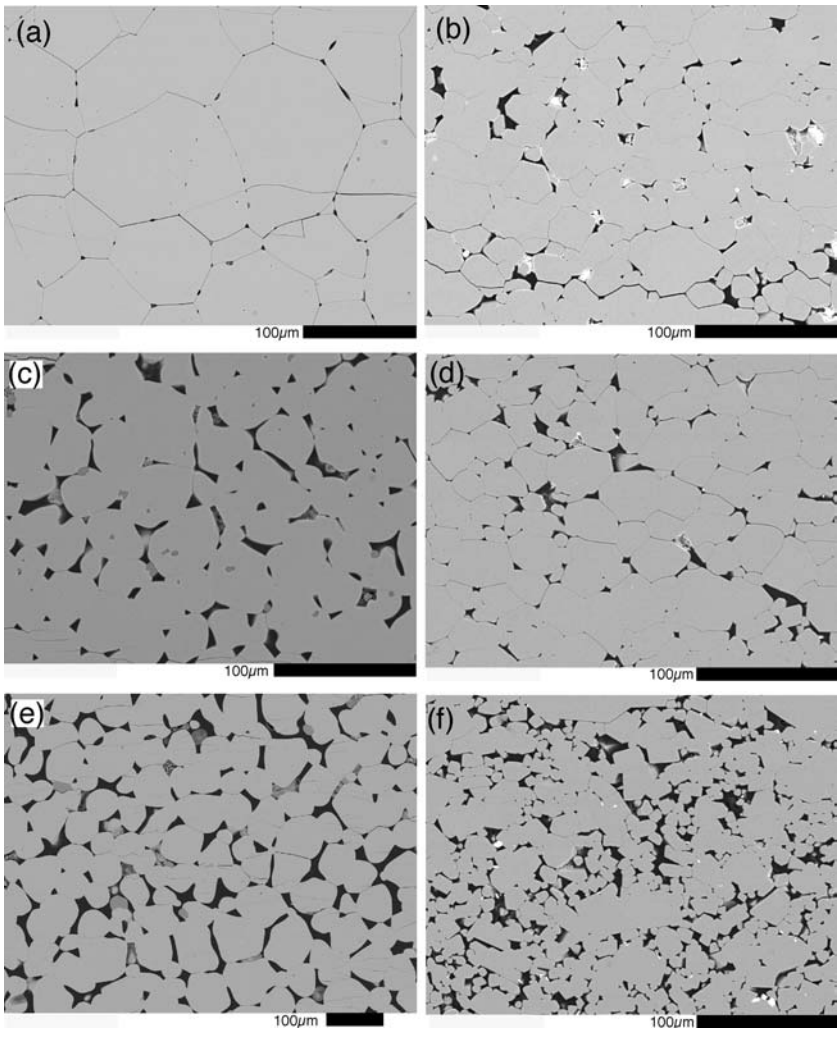

Fig. 2 Electron images of the polished section for fluorite–H_2O (**a**, **c**, **e**) and quartz–H_2O (**b**, **d**, **f**) system with various liquid volume fraction. **a** $\phi = 0.007$ (Image No. 12bfr2). **b** $\phi = 0.038$ (Image No. 19bfr2). **c** $\phi = 0.072$ (Image No. 8bfr1). **d** $\phi = 0.046$ (Image No. 12afr6). **e** $\phi = 0.129$ (Image No. 9dfr1). **f** $\phi = 0.176$ (Image No. 5bfr5)

grain growth (Karato 1989), growth rate of grains for the samples with low ϕ is faster than that with high ϕ. For this reason, a number of analyzed grains for the samples with low ϕ were restricted. However, the effect of analyzed grain numbers on F, ψ and ϕ is likely to be small for the systems with little faceting, because the liquid distribution is quite uniform. The results of image analysis are summarized in Table 1.

Results

F values

Figure 6 shows the measured F value versus liquid volume fraction (ϕ) relationships for all systems. The F value generally tends to increase monotonically with increasing ϕ independent of dihedral angle. The log F versus log ϕ plot for all systems represents that the data for each system can be well fitted by power law except for the systems characterized by low F value (Fig. 6b). The tendency is unclear for the little-faceted systems because of the large analytical error caused by low degree of faceting. Extrapolating the data for moderate and strongly faceted systems suggests that faceting persists at lower liquid fractions. For the olivine-basalt and partially molten lherzolite systems, the F values become nearly constant (~0.4) at $\phi > 0.15$. As ϕ decreases, the F values also tend to decrease. The F value becomes larger in the following order: fluorite, calcite, olivine, quartz, tremolite and clinopyroxene. The F values for the partially molten lherozlites are almost same as those for the olivine-basalt system.

Two-dimensional grain and PSDs

Grain size distributions (GSD) are variable and depend on the grain growth mechanisms. Grain growth is generally driven by a reduction of interfacial energy. The coarsening of single phase is usually described as normal grain growth, while the growth of dispersed grains in a solid or liquid matrix is usually described as Ostwald ripening. The GSD for Ostwald ripening is characterized by Lifshitz–Slyozov–Wagner (LSW) distributions with a peak skewed toward larger particle sizes, a tail extending

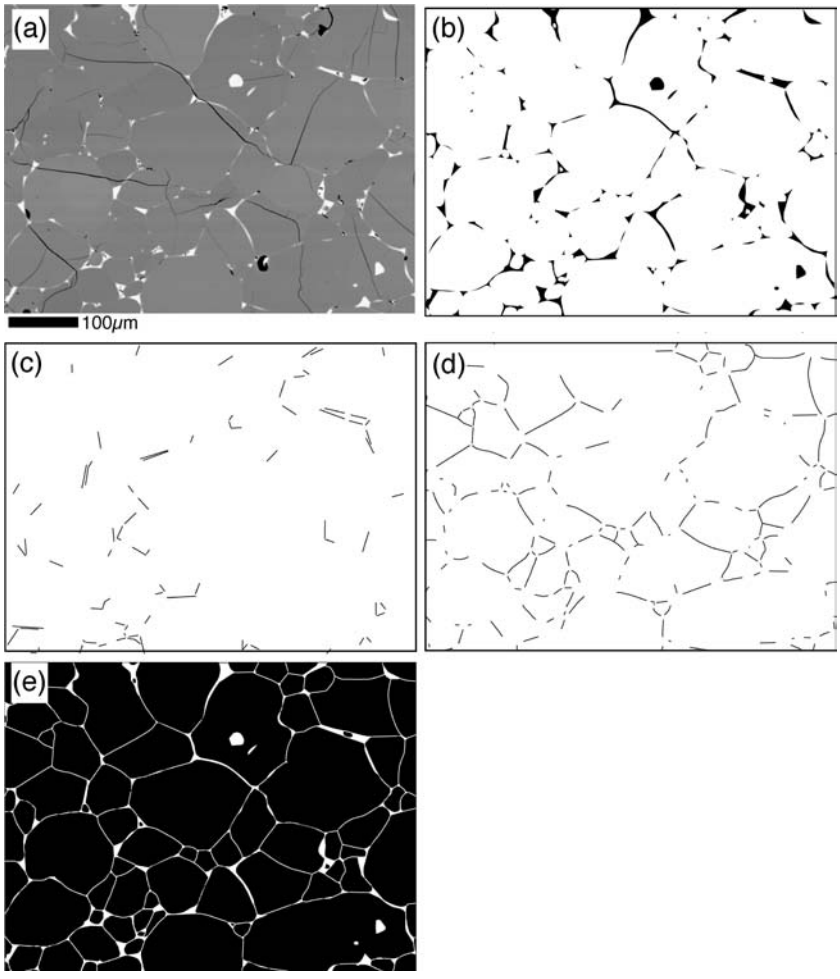

Fig. 3 An example showing analytical procedures of electron image. **a** Back scattered electron image of olivine-basalt system (Image No. FDP9-7). **b** Traced melt pools from the same area of (**a**). **c** Traced facet boundaries on the pore walls from the same area of (**a**). **d** Traced grain boundaries from the same area of (**a**). **e** Traced grain shapes from the same area of (**a**)

to the smaller particle sizes with increasing time and a sharp cut-off at particle sizes about 1.5 ($10^{1.2}$) or 2 ($10^{1.3}$) times the average size for interface-controlled or diffusion-controlled Ostwald ripening, respectively (Lifshitz and Slyozov 1961; Wagner 1961). Although our systems with low liquid fraction are not true for both grain growth mechanisms, the GSDs observed in this study are compared to the distributions obtained from the above theories.

Figure 7 shows representative log GSDs for all systems with the similar liquid volume fraction (5–6 vol.%). The GSDs are slightly influenced by the degree of faceting. The GSD of the little-faceted systems are similar to the LSW distributions. The shapes of the GSD are invariable against ϕ (Fig. 8a). Moderate-faceted systems show two different GSDs dependent on θ (Fig. 7b). The GSD of the olivine-basalt system with a low θ (34°) is quite similar to the LSW distribution as well as to the distribution in the little-faceted systems, whereas those of the quartz–H_2O system with a relatively large θ (55°) approach the log normal distribution. As ϕ increases, the GSDs of the quartz–H_2O system become broader (Fig. 8b). In the case of the strongly faceted systems, the GSDs also show the log normal distributions. The tremolite–H_2O fluid system with a lower θ (35°) shows a somewhat skewed peak in comparison with the clinopyroxene–H_2O system. Thus it is concluded that the GSDs generally change from the LSW to the log normal distribution as F and/or θ increase. Grain growth for faceted interfaces between crystal and melt is limited by surface reactions. In this case, the GSDs have a peak at the mean grain size and a cut-off at sizes about 2.5 ($10^{1.4}$) times mean grain size (Bennema and van der Eerden 1987). The GSDs of the faceted systems tend to be consistent with it rather than the LSW distributions.

For all systems, the average apparent pore size normalized by the average grain size fundamentally increases with increasing ϕ (Table 1). The increasing rate is similar for each system, suggesting that there is no distinct trend with F and/or θ. Analysis of apparent log PSD on polished sections is a quite simple but effective method to assess heterogeneity of pore distribution. Figure 9 shows the apparent PSD for pores with variable θ on a random intersection without any consideration of interaction with neighboring triple junctions and corners based on the method of Wark et al. (2003). Although the PSDs are not useful to evaluate the homogeneity of liquid distribution if ϕ is high enough to join the adjoining triple junction each other, when ϕ is

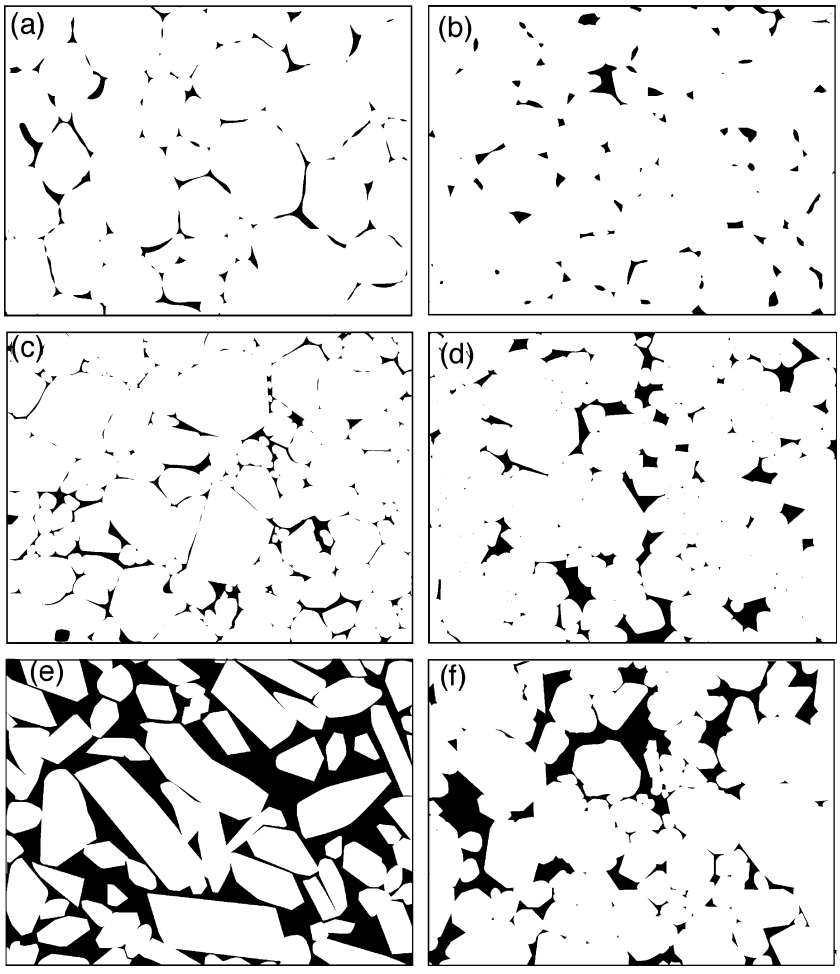

Fig. 4 The binary images showing liquid distribution constructed by manually tracing the crystal-liquid boundaries to produce a black and white bit map. The analyzed area corresponds to images in Fig. 1. **a** Fluorite–K-rich silicate melt system. **b** Calcite–H_2O system. **c** Olivine-basalt system. **d** Quartz–H_2O system. **e** Tremolite–H_2O system. **f** Clinopyroxene–H_2O system

low, the deviation of the PSD from the ideal system with constant grain size is helpful to evaluating the uniformity of the liquid distribution of the system. The apparent PSDs are characterized by log normal distribution and when θ is low, frequency of larger size is somewhat higher.

Figure 10 shows the PSDs with $\phi = \sim 0.05$. The PSDs are normalized by the average grain size to consider a relationship between maximum pore size and the average grain size. The shape is the same regardless of whether the normalized factor is an average pore size or an average grain size. The PSDs are controlled by the degree of faceting. The PSDs of little-faceted systems are approximated by the log normal distribution with a sharp peak near the center of distribution or slightly skewed toward the larger pore size (Fig. 10a–c). The PSDs are quite similar to the PSD obtained from the ideal system, suggesting that little-faceted systems have uniform pore distributions.

Moderately-faceted systems show broader PSD: pores larger than the average grain size appear. The PSDs of the olivine-basalt and partially molten lherzolite systems are quite similar to each other and the peaks of the PSDs are still located near the center of the distributions (Fig. 10d–f). However, the PSD of the quartz–H_2O system with a relatively large dihedral angle (55°) is strikingly different from the olivine-basalt system in spite of the nearly same degree of faceting. The PSDs are far from the log normal distribution (Fig. 10f). This pattern of peak broadening, which is characterized by both the higher frequency of smaller pore sizes and the appearance of larger pore sizes, is consistent with the observed pore geometry showing shrinkage of triple junction tubes and development of large pores. The large deviation from the log normal distribution suggests that the quartz–H_2O system has an inhomogeneous liquid distribution (Wark and Watson 1998).

Strongly-faceted systems (Fig. 10g–h) show different PSDs dependent upon θ. The PSD of the tremolite–H_2O system with low θ has a broad distribution with a peak near its center (Fig. 10g), whereas the PSD of the clinopyroxene–H_2O system with large θ are quite similar to that of the quartz–H_2O system (Fig. 10f). In contrast, the distribution of pores in the tremolite–H_2O system suggests little development of large pores and relative homogeneity. Despite the numerous differences between strongly- and moderately-faceted systems, they display similarly broad PSDs.

Figure 11 shows the effect of ϕ on the PSDs for calcite–H_2O system and quartz–H_2O system which are

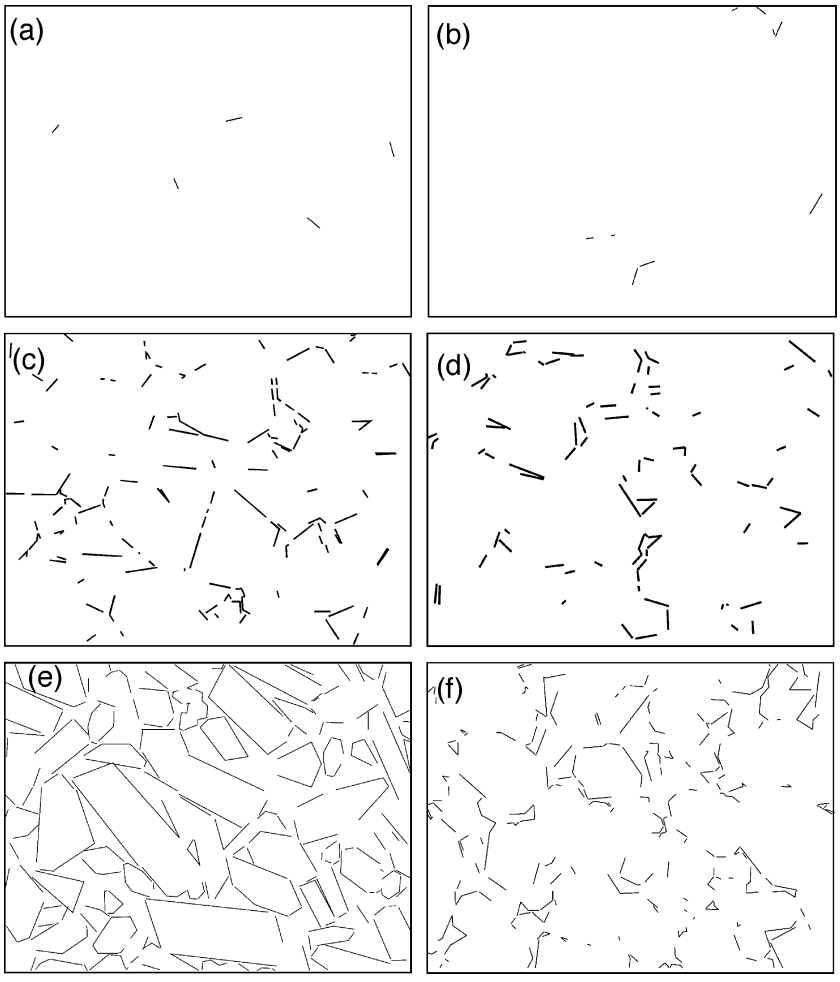

Fig. 5 Images showing facet boundary. Visually straight interphase boundaries were also manually traced to determine the F value. The analyzed area corresponds to images in Fig. 1. **a** Fluorite–K-rich silicate melt system. **b** Calcite–H_2O system. **c** Olivine-basalt system. **d** Quartz–H_2O system. **e** Tremolite–H_2O system. **f** Clinopyroxene–H_2O system

characterized by different degrees of faceting. The shapes of the PSD for the calcite–H_2O system are invariable against ϕ and have a slightly skewed peak towards larger pore sizes and a peak shifts toward the larger pore size with increasing ϕ (Fig. 11a–c). For the quartz–H_2O system, the peak of the PSDs skews toward the smaller pore sizes and a tail extends to the larger pore sizes (Fig. 11d–f). As ϕ increases, a tail of the PSDs extends to the larger pore size and a peak abruptly shifts toward the larger size.

Discussions

Interpretation of dependence of F value on ϕ

Faceting corresponds to crystallographically-controlled faces with lower interfacial energy than that produced by the curved interfaces. The orientations of minimum interfacial energy per unit area are crystallographic planes of low Miller indices (Laporte and Provost 2000 and references therein). The equilibrium interface structure should be considered in terms of a plot of the interfacial energy against grain boundary plane normal orientation (Wulff or γ-plot) and a corresponding equilibrium crystal shape (e.g., Herring 1953). A cusp in the γ-plot corresponds to a singular plane in the equilibrium shape. Herring (1953) has shown that at equilibrium, the ratio of distances between each facet is a measure of their interfacial energy ratio. Due to changes in physical conditions, a faceted interface with the shallowest cusps of the surface energy function may transform to a curved surface. When all singular planes corresponding to cusps in the γ-plot undergo roughening, the equilibrium shape will have no slope discontinuity (defaceting). Considering a single crystal completely surrounded by a given liquid phase, then the degree of faceting for the crystal can be defined by an intrinsic F value for one solid grain (F_{abs}: absolute F value), corresponding to the Wulff shape at a given physical condition.

The degree of faceting is controlled by temperature, pressure and liquid composition. For example some researchers have demonstrated that the equilibrium shape of liquid inclusions embedded in a solid matrix changes from a faceted to spheroidal shape (faceting/defaceting transition) with increasing temperature (e.g., Dahmen et al. 1997; Garbrisch et al. 2001). The transition temperature depends on the bond energy in the plane of the facet (e.g., Bennema and van der Eerden 1987).

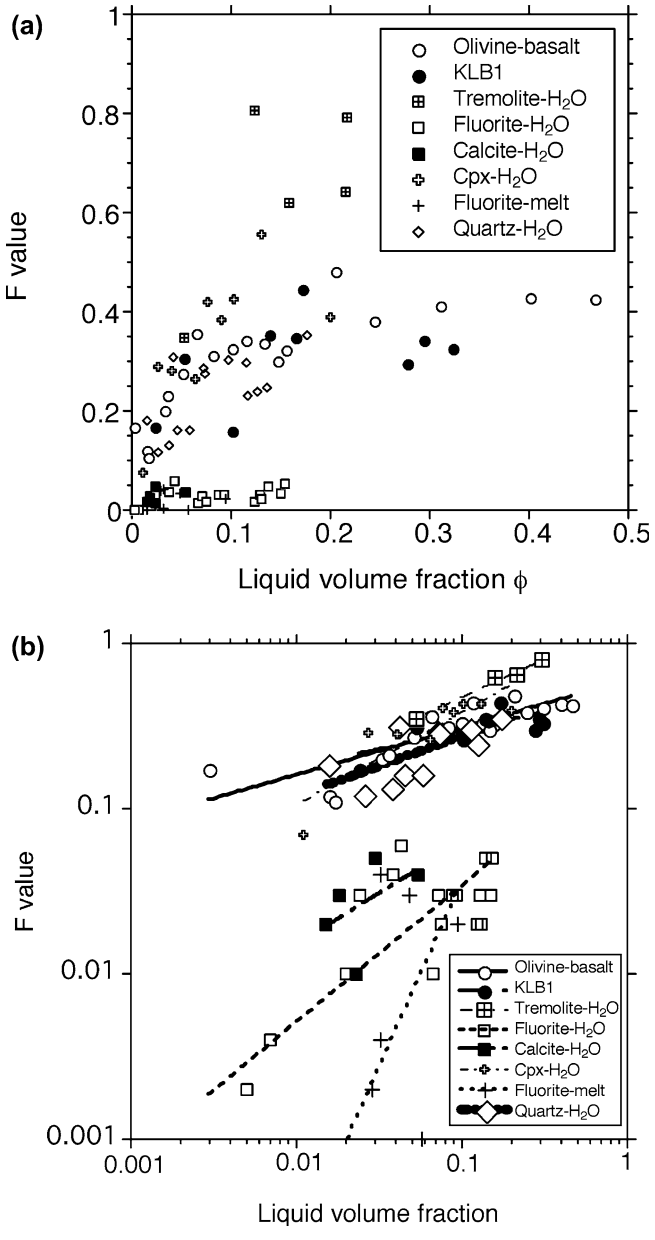

Fig. 6 Effect of liquid volume fraction (ϕ) on degree of faceting (F) for all systems. **a** *Linear plot*: Note that the F values generally increase with increasing ϕ. **b** *Log* ϕ–log F plot: note that relationship between ϕ and F can be well fitted by power law. For moderately- and strongly-facted systems, extrapolations of power law fitting suggest that even if the porosity is very small, a certain amount of faceted boundary between crystal and liquid could be present

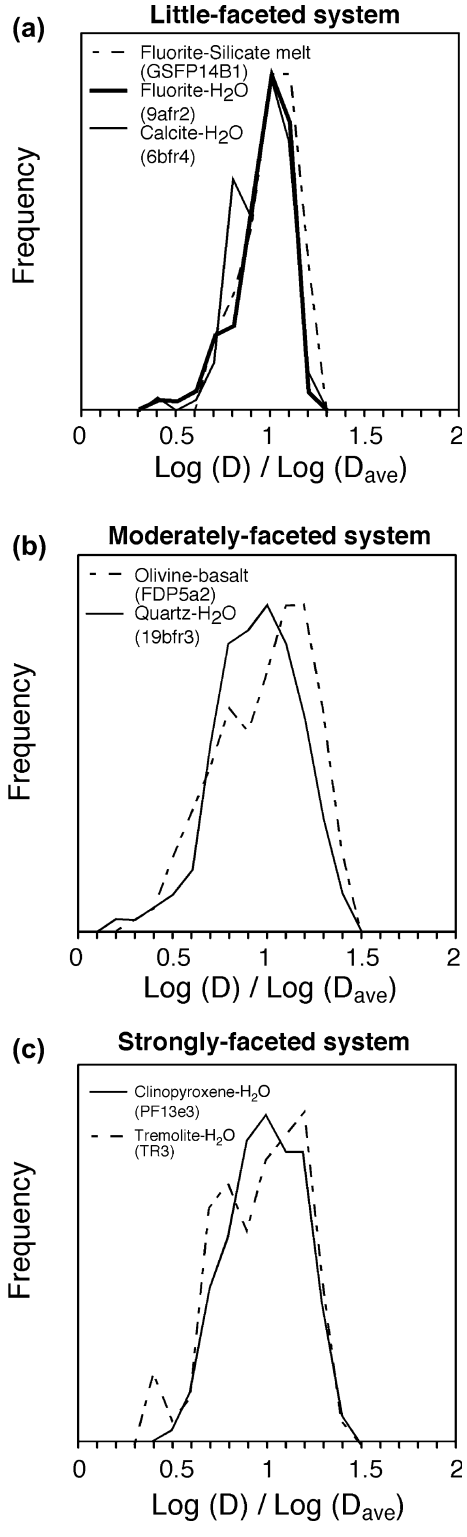

Fig. 7 Representative log grain size distributions (GSDs) normalized by average grain size for several systems with different degrees of faceting. **a** Little-faceted systems. **b** Moderate-faceted systems. **c** Strongly faceted systems

The present results obtained from the calcite–H_2O system show no evidence of development of rational faces although calcite is considered a more anisotropic mineral than fluorite. Therefore, the development of planar crystal–liquid interfaces may not neccessarily be correlated to only an empirical criterion of the degree of anisotropy of interfacial energies.

As shown in Fig. 6, the degree of faceting (F) tends to increase with increasing ϕ. First we consider the ideal case that crystallographic orientations of grains are random and the F_{abs} value is constant at a given experimental condition. The probability that facets

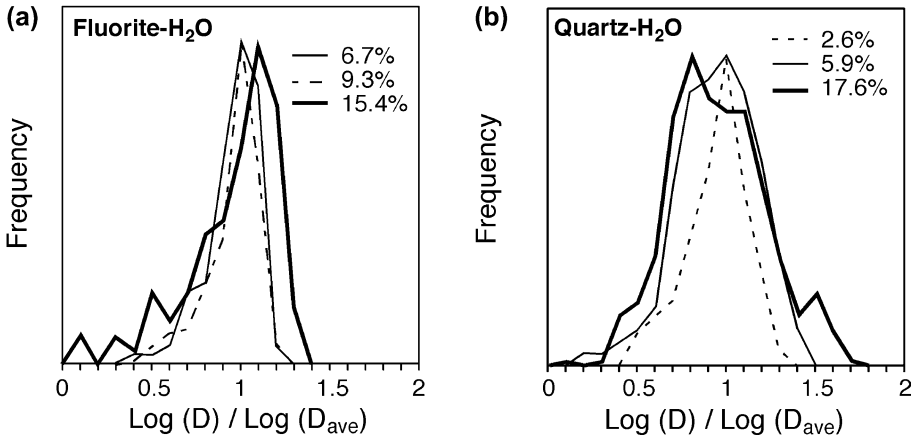

Fig. 8 Normalized log GSDs as a function of liquid volume fraction (ϕ). **a** Fluorite–H_2O system. **b** Quartz–H_2O system

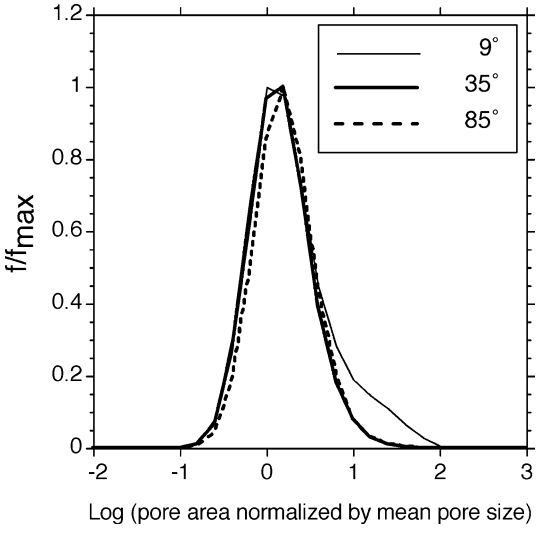

Fig. 9 Histograms of log pore size distributions (PSDs) calculated in numerical experiments for 9, 35 and 85° triangular prisms based on the results of Wark et al. (2003)

occupy the total crystal surface corresponds to the F_{abs}. If the crystal–liquid surface was chosen randomly on the crystal with a singular F_{abs}, the probability for appearance of facet on the crystal–liquid interfaces depends on only F_{abs} independently of ϕ. Therefore, F should maintain a constant value against variable ϕ.

Why do the F values depend on ϕ? One simple interpretations is that the dependance is merely an artifact of imaging resolution and scale. The identification of rational flat faces is more difficult for images with lower ϕ because higher magnification is required for accurate determination of F. We may miss identifying some facets at a very low fluid fraction. Thus F values may be too small at low ϕ. Even if some facets are not observed, they must make up a very small portion of the pore wall area (i.e., very low F), to be consistent with the observations made on systems with higher ϕ. In other words, even if some facets are missed at very low ϕ, this will not change our results. It seems likely that our data show that F is not underestimated from low ϕ images, but instead decreases with ϕ. Likewise, the TEM work of Cmíral et al. (1998) suggests that F is reduced with very low melt fractions.

The dependence of F on ϕ may result from lower surficial energy produced by rotating the interfaces due to grain rotation with larger fluid concentrations. Because the solid–liquid interface increases with ϕ, the continuous, self-supporting skeleton of solid grains breaks down when the contiguity falls to a value of 0.15–0.2. Considering that the grains are more likely to rotate as ϕ increases, this process would enhance an increase of F with ϕ. However, our data suggest that as ϕ decreases, the value of F decreases significantly even for the strongly faceted system. It is unrealistic to produce this huge variation only by grain rotation.

The most probable explanation is that changes in interfacial energy due to the presence of facets stabilize rounded pore walls rather than rational faces at low ϕ. When the total interfacial energy per unit area for the curved interface is lower than that for the flat face, the curved interface is stable. The crystal–liquid surface can be described by three components, including the curved solid–liquid interfaces, flat solid–liquid interfaces and edges (the intersection between flat and curved interfaces). Dependence of the F values on ϕ means that the interfacial energy per unit area also depends on ϕ. We consider two possibilities for interfacial energy changes with decreasing ϕ: In the first, we consider that pore geometry at triple junctions for different ϕ is self-similar. The curvature of curved pore wall is expected to be constant regardless of ϕ, although pore size decreases with decreasing ϕ at a constant dihedral angle. In contrast, the interfacial energy of the faceted portion of the wall is also constant. The edges have higher energy compared with the other solid–liquid interfaces. Although the edge energy increases with the intersection angle, edge energy should be constant based on an assumption of self-similarity. However, density of edges per unit area of crystal–liquid interface should be larger. Then smooth curved surfaces may be more stable than surfaces composed of facet and curved interfaces. As ϕ

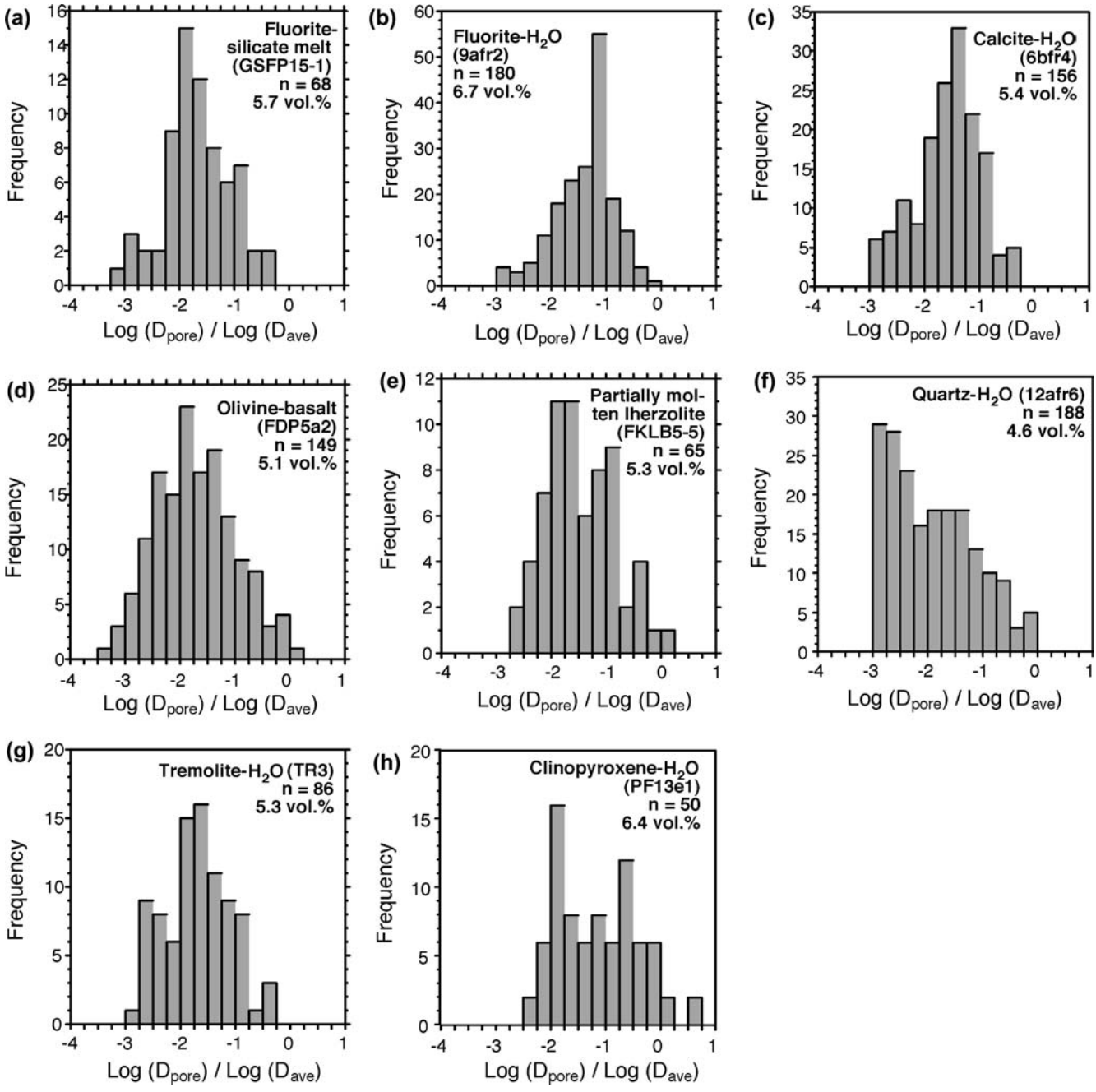

Fig. 10 Histograms of log PSD normalized by average grain size for several systems with different degrees of faceting. Left and right side figures correspond to the systems with low and high dihedral angles, respectively. The *top three figures* are representative histograms of little-faceted systems: **a** fluorite–silicate melt system, **b** fluorite–H_2O system and **c** calcite–H_2O system. The *middle three figures* are representative histograms of moderate-faceted systems: **d** olivine-basalt system, **e** partially molten lherzolite and **f** quartz–H_2O systems. The *bottom two figures* are representative histograms of strongly faceted systems: **g** tremolite–H_2O system and **h** clinopyroxene–H_2O systems

decreases, the increased edge density may induce surface roughening due to the existence of an energy barrier that needs to be overcome before particles attain their equilibrium shape. If an edge on the crystal surface elastically interact with the nearest edge, the shape of pore wall favors rough surfaces rather than facets (Jayaprakash et al. 1984; Mullins and Rohrer 2000; Garbrisch et al. 2001).

Next consider the case that interfacial energy of curved surface becomes larger with decreasing pore size as ϕ decreases. The edge energy increases with decreasing ϕ, because the intersection angle becomes larger. This tendency would enhance a formation of the curved surface to minimize the interfacial energy per area. In either case, then facets may become unstable when the system has low ϕ.

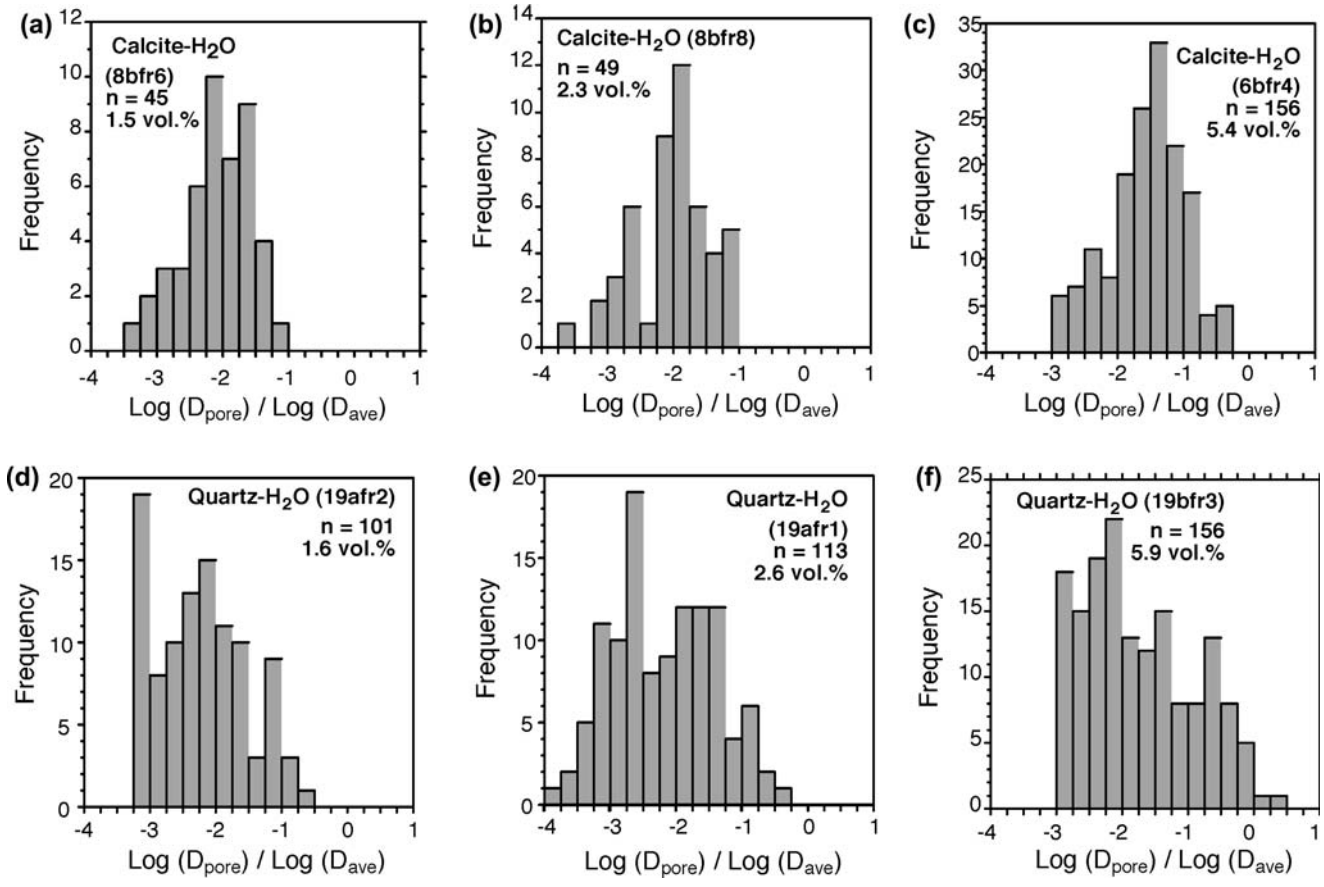

Fig. 11 Histograms of log PSDs for calcite–H_2O system (**a**–**c**) and quartz–H_2O systems (**d**–**f**) as a function of ϕ

Mechanism of liquid re-distribution due to faceting

The present results demonstrate that segregation of liquid into large pores occurs in the partially faceting systems with both curved and faceted pore walls, whereas little-faceted and strongly-faceted systems show no clear evidence of liquid segregation. What are the mechanisms responsible for liquid segregation of the partially-faceted system? It is expected that liquid in a system redistributes itself to achieve a minimum interfacial energy. Based on the concept of interfacial energy minimization, we now consider if the observed inhomogeneity of liquid distribution can be attributed to any of the following: (1) a minimum-energy fluid fraction in a system consisting of crystals and liquid, (2) a presence of GSD and (3) a development of faceted planar faces at the pore wall.

First we consider a liquid segregation mechanism in an ideal system consisting of mono-sized crystals with isotropic interfacial energy. The minimum energy fluid fraction (ϕ_m) establishes a minimum in interfacial energy for the liquid–crystal system according to dihedral angle (θ), constant mean curvature (κ) and grain packing geometry (Jurewicz and Watson 1985; Park and Yoon 1985). For fluid fractions up to ϕ_m, fluids are expected to infiltrate; if a fluid fraction over ϕ_m is initially contained in the rock, the excess fluid should be expelled. Therefore, if the system has a fluid fraction larger than ϕ_m, a large pore may be formed by segregation of excess liquid. The value of ϕ_m decreases with increasing θ assuming that the grain packing geometry is invariable against the liquid volume fraction. For example, the value of ϕ_m for the system having the grain packing with 12 coordination numbers decreases from 0.23 at $\theta = 0°$ through 0.10 at $\theta = 45°$ to 0.03 at $\theta = 60°$. If it is true for our systems, the segregation into large pore is likely to occur for the system with a high θ. However, the fluorite– and calcite–H_2O systems characterized by a high θ values show no remarkable evidence of segregation. On the other hand, the segregation occurs at a fluid fraction less than ϕ_m for the tremolite–H_2O fluid system ($\sim$0.15) and the quartz–H_2O system ($\sim$0.03). These observations are inconsistent with the prediction from those predicted by the minimum energy fluid fraction for the ideal system.

The concept of the minimum energy fluid fraction is not satisfied by the requirement of uniform κ and θ if the grain size is not uniform (Wark and Watson 2000). When a system with both fine- and coarse-grained regions maintains constant θ, the further constraint of uniform κ requires that the fluid partitions into the region consisting of the fine grains or around individual

small grains. In our experiments, the GSDs for the moderately-faceted systems show higher frequency of smaller grains, which should enhance the local segregation. However, there is no clot of fine grains completely surrounded by much larger grains. The grain size averaged over the scale of several grains seems to be uniform in a texturally equilibrated system. Rather the large pores are usually surrounded by or in contact with at least one single large grain with flat crystal/liquid interface.

Redistribution of fluid can be considered in terms of the minimization of interfacial energy due to facet formation. Three critical observations characterize the liquid distribution of texturally equilibrated rocks: (1) F decreases with decreasing fluid fraction, (2) PSD changes with fluid fraction—the higher the fluid fraction, the broader the pore-size distribution and the greater the amount of fluid segregation (characterized by width of PSD) and (3) fluid segregation is greatest in partially faceted systems with high dihedral angle. In a system that exhibits no facets ($F = 0$ at all ϕ), an increase in fluid fraction results in an increase in the size of all pores, and in a decrease in pore-wall curvature. In the partially faceted system, in which both rounded surfaces and facets are stable ($0 < F < 1$), pores that happen to be surrounded by grains with favorable crystallographic orientations (see Fig. 12) will start to develop facets. Once they start to develop facets, these same pores can continue to grow larger while other (non faceted) pores remain the same size (or perhaps decrease in size) and retain the same curvature (see Fig. 13). In other words, the PSD broadens.

Why would it happen this way? This minimizes the total free energy of the system by: (a) decreasing the total pore wall area for a given volume of rock (putting a given volume of fluid into a single large pore instead of into several triple junction tubules results in lower pore-wall area), (b) adding flat (low-energy) pore walls rather than adding additional curved (higher energy) pore walls, (c) possibly allowing the bulk of the system to maintain its ''equilibrium fluid fraction'' (fluid in excess of the equilibrium fluid fraction may go into pores bounded by faceted surfaces). In the partially-faceted systems, the equilibrium fluid fraction may be defined based on only the assumption that the curvature of the crystal/fluid-curved interface (exclusive of flat interfaces) is uniform. In this case, the equilibrium fluid fraction in the faceted system is significantly lower than that in the ideal system and depends on the degree of faceting.

Another way to look at it is to consider that partially faceted pore walls provide greater ''geometric flexibility'' to allow fluid segregation. In fact, in the absence of facets, such segregation is not possible. For a system with no facets, the requirements of uniform pore-wall curvature and uniform (approximately) dihedral angle result in relatively uniform fluid distribution on the scale of several grains. In the presence of facets, however, it becomes possible to produce a non-uniform fluid distribution characterized by segregating fluid into large

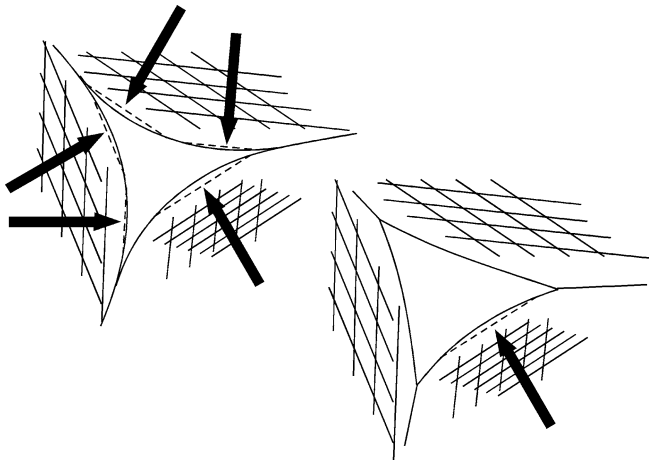

Fig. 12 The pore on the left, with low dihedral angle, has multiple pore wall segments (*arrows* and *dotted lines*) that correspond with planes favorable for development of facets. The pore on the right, with high dihedral angle, has only one segment corresponding to low-energy faceted surface. This illustrates why systems with low dihedral angles may develop faceting on a larger number of pores, which in turn results in less fluid segregation (added fluid is simply distributed among a larger number of pores, assuming that added fluid only goes into pores with facets). Systems characterized by high dihedral angle, in contrast, will have few pores with walls corresponding to low energy surfaces. Because most fluid will go into these few pores, the fluid becomes increasingly segregated with increasing fluid fraction

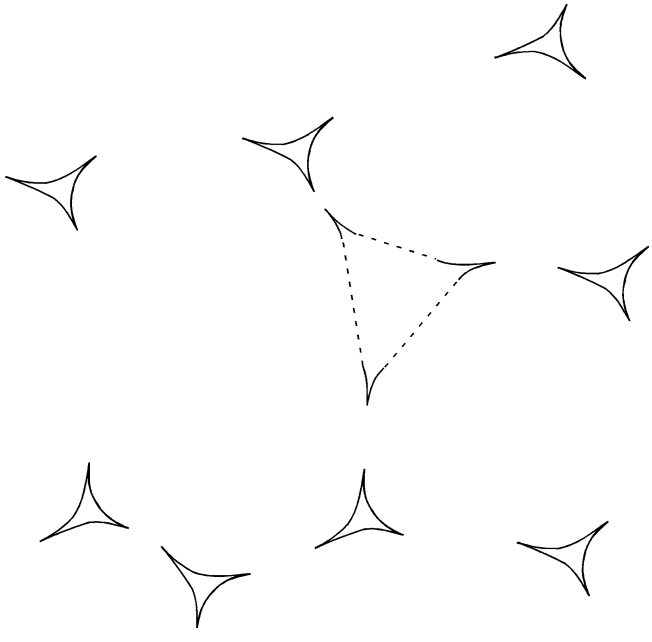

Fig. 13 Illustration showing a hypothetical system with only one pore that has pore wall segments parallel to low-energy (facet-forming) crystallographic planes. As fluid fraction increases, the additional fluid can be (mostly) accommodated by this single pore by increasing the area of the flat walls, without significantly changing the area or curvature of the curved pore walls. This may explain why F increases with fluid fraction. As shown in Fig. 12, a system like the one shown here, with low dihedral angle, would probably develop facets on many pore walls

pores, while maintaining uniform pore-wall curvature on the segments that are curved (Fig. 12). Curved pore walls may still be present where two grains join, but these curved-pore-wall segments can be connected by facets and these faceted segments can be virtually any length (up to the size of the grain, at least). So, the pores with faceted walls can grow, while pores with only curved walls will remain the same size.

This also explains why we documented greater segregation for partially faceted systems with the higher dihedral angles. If the dihedral angle is high (right diagram of Fig. 12), the pore walls have lower curvature (imagine a triple junction with a dihedral angle of 60°: the curvature will be zero), and only rarely will some segment of a pore wall be parallel to a favorable crystallographic orientation for faceting. The few pores that start to develop facets will increase in size, and with increased fluid fraction. In contrast, if the dihedral angle is low (left side Fig. 12), the pore walls are more curved (imagine a triple junction with dihedral angle of 10°), and the various pore-wall segments correspond to many different crystallographic orientations, increasing the odds that for any single pore there will be at least one pore-wall segment parallel to a favorable orientation. Consequently, for low dihedral angle, faceting will be more common (not restricted to only a few pores, that is). Any increase in fluid fraction is taken up by development of facets on many pores at once. Again total energy is probably reduced by accommodating the fluid in pores with flat rather than curved walls. But because there is a higher proportion of pores with faceted walls, the amount of fluid segregation appears to be less.

Effect of faceting on permeability

The permeability of liquid phase in porous rocks has been commonly calculated based on some simplified assumptions about the pore geometry. For example, von Bargen and Waff (1986) assumed mono-sized tetrakaidecahedral grains with isotropic energies in order to predict the permeability–porosity relations as a function of θ. The liquid phase forms a regular network consisting of tubules along three-grain edge intersections and four-corners (e.g., Bulau et al. 1979). The permeability k for this model is ($\phi < 0.03$):

$$k = \Delta q \frac{d^2\phi^2}{144\pi\sqrt{2}}, \tag{5}$$

where d is the grain size and Δq is a geometric correction factor depending on the cross-sectional shape of the tubes: Δq is equal to 1 for circular tubes and to ~0.4 for sided-sided tubes with $\theta = 30°$. For $\theta < 60°$, k decreases smoothly with decreasing ϕ as a function of ϕ^2. For $\theta > 60°$, k decreases monotonically with decreasing to ϕ_m (percolation threshold). For this model, an increase of ϕ is accommodated by an increase of the tube diameter, although the overall geometry is invariable. These k–ϕ^2 relationships have been widely used to model the segregation of low melt fractions in the upper mantle.

Wark and Watson (1998) reported an empirical k–ϕ relation by direct measurement of permeabilities for synthesized porous quartzite using a transient pulse decay method. This relationship can be described by (modified after Liang et al. 2001)

$$k = \frac{d^2\phi^3}{270}. \tag{6}$$

The empirical permeabilities are lower than those predicted from von Bargen and Waff (1986) by a factor of 5–10 for the same ϕ, with the greatest differences at the lowest porosities. Although the pore geometry for the analyzed systems is approximated well by a triple junction tube network based on a relation between grain boundary wetness and ϕ (Yoshino et al. 2005), a slope of power-law function for permeability–porosity relation agrees well with 3 rather than 2. Thus we should note that triple junction tube network in the real rocks does not correspond to the "ideal" system. In general, natural rocks with complex pore structures and a wide range of pore sizes and shapes are also characterized by a cubic dependence of permeability on porosity (e.g., Bourbié and Zinszner 1985). The main factor likely to influence permeability seems to be the difference of pore microstructure between real and ideal materials.

One notable difference is the development of faceting in actual rocks. The deviations of the permeabilities for synthesized porous marble characterized by little faceting from the results of von Bargen and Waff (1986) are smaller (a factor of ~2) than that for quartz–H_2O system (Wark and Watson 1998). Furthermore, Price et al. (2006) reported that the permeabilities of the tremolite–H_2O system, characterized by strong faceting, have a percolation threshold even though θ is less than 60°. These k–ϕ relations indicate that degree of faceting in a given system strongly affects the permeability.

The present results also suggest that the development of faceting occasionally leads to a remarkably inhomogeneous pore distribution. In particular, the quartz–H_2O system, characterized by moderate faceting, distinctly shows the development of large pores surrounded by four or more grains and the corresponding shrinkage of triple junctions. The PSDs of the quartz–H_2O system shows high frequency of small-sized pores, suggesting shrinkage of triple junctions compared to the other systems. Therefore, the radius of triple junction becomes lower than that of the ideal model. Although large pores surrounded by four or more grains contain a significant fraction of total ϕ, they would not be interconnected with each other at low ϕ. Consequently, the interconnection of the liquid phase in the system with $\theta \leq 60°$ would be established by a network of triple junction tubes of smaller radius connecting the isolated large pores (Fig. 14). Since the cross sectional area of triple junction tube controls the permeabilities in quartz

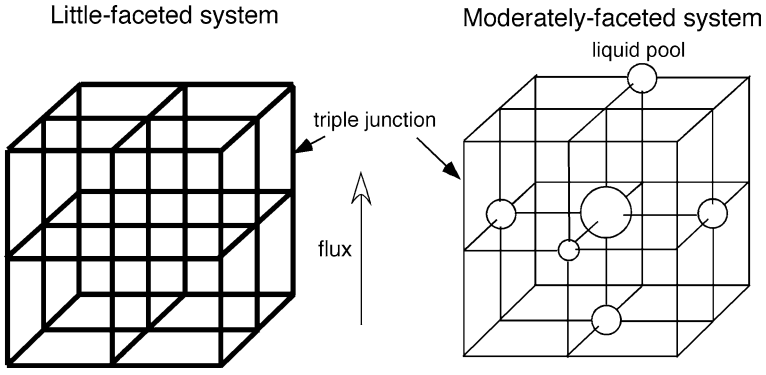

Fig. 14 Schematic cartoons of triple junction network for faceting (*left*) and moderate-faceted (*right*) systems. For moderate-faceted system, radius of triple junction tube is smaller than that for little-faceted system due to the formation of large pores at the same ϕ. This behavior leads to low permeabilty of moderate-faceted system

aggregates, for low ϕ, Eq. 5 may overestimate by orders of magnitude the permeability of quartz aggregates because liquid mostly partitions into the large pores. Relationships of k–ϕ for porous quartzite show no evidence of a permeability threshold, where permeability suddenly increases with increasing ϕ (Wark and Watson 1998). This suggests that the isolated large pores that contain most of the liquid phase continuously become interconnected with increasing ϕ, and/or the cross-sectional area of each triple junction tube monotonically increases with increasing ϕ. The effect of increasing porosity exponent from 2 to 3 in the k–ϕ relationship suggests that as ϕ decreases, effective triple junction radius becomes smaller, faster than it does for the ideal model. This conclusion is supported by PSD peak shift to larger size for quartz–H_2O system relative to the little-faceted system (see Fig. 7).

For the tremolite–H_2O systems showing extensive faceting, the deviations of a k–ϕ relation from the ideal model may be of a different origin from that of the quartz–H_2O system. In fact the PSD of the tremolite–H_2O systems shows a sharp peak at the center of distribution that suggests more homogeneous distribution rather than the quartz–H_2O system. On polished sections, triple junction tubes for this system are not common. Rather pores surrounded by four or more grains with faceted pore walls are dominant. Therefore, the pore distribution is probably quite different from a network along the intersections of three-sided grain edges. The k–ϕ relation of the tremolite–H_2O system showing apparent ϕ_m ($=0.04$) suggests that triple junction tubule is plagued by a truncation of the rational faces due to extensive development of facets. Furthermore, most pores are likely to become isolated as the degree of faceting increases. As a result, the strongly-faceted systems are impermeable at low ϕ.

Based on the observations of the size difference between triple junction geometries and melt pools surrounded by more than four grains for the olivine-basalt system (e.g., Waff and Faul 1992; Faul et al. 1994; Faul 1997; Cmíral et al. 1998), Faul and coworkers interpreted that melt distributions consist of small proportion ($< 15\%$) of triple junction tubes and large proportion of disk-shaped layers on two grain boundaries. Faul (1997, 2001) proposed that the interconnection of disk-shaped pore produces the permeability jump at ϕ_m. However, Wark et al. (2003) demonstrated that as melt fraction increases, two-dimensional slices through the pore network may appear "disk-shaped", when in fact the pore network is composed of triple junction tubules. Furthermore, Yoshino et al. (2005) suggested that the pore geometry for the olivine-basalt system is approximated well by a triple junction tube network based on a relation between grain boundary wetness and ϕ. A relationship between F and ϕ of the quartz–H_2O system is quite similar to that of the olivine-basalt system. Wark and Watson (1998) could not find any evidence of the percolation threshold. Therefore, it is expected that the basaltic melt in olivine aggregate also has no permeability jump.

Conclusion

We examined the effect of faceting at the solid–liquid boundary on pore geometry in texturally equilibrated melt- or fluid-bearing synthetic materials that serve as good analogs for rocks with variable dihedral angles and degree of faceting using image analysis of back-scattered and secondary-electron images. For all systems, the degree of faceting (defined by the ratio of the flat interface length at the pore wall to the length of total interfacial boundary between solid and liquid) increases monotonically with increasing liquid volume fraction. Little-faceted systems show uniform pore distribution, also shown by the log normal distribution of the PSD. The quartz–H_2O (moderately faceted) system shows development of large pores surrounded by faceted pore walls and complementary shrinkage of triple junction tubes, whereas the tremolite–H_2O (strongly-faceted) systems with a low dihedral angle show no evidence of shrinking triple junction tubes, although most pores are surrounded by faceted pore walls. The presence of facets relaxes constraints imposed by requirement of uniform curvature and single dihedral angle. This, in turn, allows for formation of pores larger than would otherwise be allowed. In the systems with the same degree of faceting, heterogeneity of liquid distribution tends to decrease with decreasing dihedral angle. For faceted systems permeability of texturally equilibrated rocks with low

liquid fraction would be reduced by the relative reduction of volume fraction of triple junction occupied by liquid, or by closure of channels along grain edges due to the truncation by facet walls.

Acknowledgments We are grateful to Y. Liang, Y. Takei and T. Hatakeyama for discussion. The comments of anonymous reviewer and U. H. Faul adided in improving the manuscript. This work was supported by the Research Fellowships to T. Y. from the Japan Society for Promotion of Science for Young Scientists. Experiments and analyses at Rensselaer Polytechnic Institute were supported by U.S. Department of Energy grant no. DE-FG02-94ER1443 to E.B. Watson.

References

Bennema P, van der Eerden JP (1987) Crystal graphs, connected nets, roughening transition and the morphology of the crystals. In: Sunagawa I (ed) Mophology of crystals. Terra Scientific Publishing Co, Tokyo, pp 1–77

Bourbié T, Zinszner B (1985) Hydraulic and acoustic properties as a function of porosity in Fontainebleau sandstone. J Geophys Res 90:1524–1532

Bulau JR, Waff HS, Tyburczy JA (1979) Mechanical and thermodynamic constraints on fluid distribution in partial melts. J Geophys Res 84:6102–6108

Cheadle MJ, Elliot MT, McKenzie D (2004) Percolation threshold and permeability of crystallizing igneous rocks: the importance of textural equilibrium. Geology 32:757–760

Dahmen U, Xiao SQ, Paciornik S, Johnson E, Johansen A (1997) Magic-size equilibrium shapes of nanoscale Pb inclusions in Al. Phys Rev Let 78:471–474

Cmíral M, Fitz Gerald JD, Faul UH, Green DH (1998) A close look at dihedral angles and melt geometry in olivine-basalt aggregates: a TEM study. Contrib Mineral Petrol 130:336–345

Faul UH, Toomey DR, Waff HS (1994) Intergranular basaltic melt is distributed in thin, elongated inclusions. Geophys Res Lett 21:29–32

Faul UH (1997) Permeability of partially molten upper mantle rocks from experiments and percolation theory. J Geophys Res 102:10299–10311

Faul UH (2001) Melt retention and segregation beneath mid-ocean ridges. Nature 410:920–923

Garbrisch H, Kjeldgaard L, Johnson E, Dahmen U (2001) Equilibrium shape and interface roughening of small liquid Pb inclusions in solid Al. Acta Material 49:4259–4269

Herring C (1951) Some theorems on the free energies of crystal surfaces. Phys Rev 82:87–93

Herring C (1953) The use of classical macroscopic concepts in surface-energy problems. In: Gomer R, Smith CS (eds) Structure and properties of solid surfaces. University of Chicago Press, Chicago, p 5

Jayaprakash C, Rottman C, Saam WF (1984) Simple model for crystal shapes: step–step interactions and facet edges. Phys Rev B 30:6549–6554

Jurewicz SR, Watson EB (1985) The distribution of partial melt in a granitic system: the application of liquid phase sintering theory. Geochim Cosmochim Acta 49:1109–1121

Karato S (1989) Grain growth kinetics of olivine aggregates. Tectnophysics 168:255–273

Laporte D (1994) Wetting behavior of partial melts during crustal anatexis: the distribution of hydrous silicic melts in polycrystalline aggregates of quartz. Contrib Mineral Petrol 116:486–499

Laporte D, Provost A (2000) The grain-scale distribution of silicate, carbonate and metallosulfide partial melts: a review of theory and experiments. In: Bagdassalov N, Laporet D, Thompson AB (eds) Physics and chemistry of partially molten rocks. Kluwer, Dordrecht, pp 93–140

Laporte D, Watson EB (1995) Experimental and theoretical constraints on melt distribution in crustal sources: the effect of crystalline anisotropy on melt connecticity. Chem Geol 124:161–184

Liang Y, Price JD, Wark DA, Watson EB (2001) Nonlinear pressure diffusion in a porous medium: approximate solutions with applications to permeability measurements using transient pulse decay method. J Geophys Res 85:5173–5189

Lifshitz IM, Slyozov VV (1961) The kinetics of precipitation from supersaturated solid solutions. J Phys Chem Solids 19:35

Mullins WW, Rohrer GS (2000) Nucleation barrier for volume-conserving shape changes of faceted crystals. J Am Ceram Soc 83:214–216

Park HH, Yoon DN (1985) Effect of dihedral angle on the morphology of grains in a matrix phase. Metall Trans A 16:923–928

Price JD, Wark DA, Watson EB, Smith AM (2006) Grain-scale permeabilities of faceted polycrystalline aggregates. Geofluids (in press)

Takahashi E (1986) Melting of a dry peridotite KLB-1 up to 14 GPa: implications on the origin of the peridotitic upper mantle. J Geophys Res 91:9367–9382

Toramaru A, Fujii N (1986) Connectivity of melt phase in a partially molten peridotite. J Geophys Res 91:9239–9252

von Bargen N, Waff HS (1986) Permeabilities, interfacial areas and curvatures of partially molten systems: results of numerical computations of equilibrium microstructures. J Geophys Res 91:9261–9276

Waff HS, Bulau JR (1979) Equilibrium fluid distribution in an ultramafic partial melt under hydrostatic stress conditions. J Geophys Res 84:6109–6114

Waff HS, Faul U (1992) Effects of crystalline anisotropy on fluid distribution in ultramafic melts. J Geophys Res 97:9003–9014

Wagner C (1961) Theorie der altering von niederschlagen durch umlosen (Ostwald Reifung). Z Electrochem 65:581

Wark DA, Watson EB (1998) Grain-scale permeabilities of texturally equilibrated, monomineralic rocks. Earth Planet Sci Lett 164:591–605

Wark DA, Watson EB (2000) Effect of grain size on the distribution and transport of deep-seated fluids and melts. Geophys Res Lett 27:2029–2032

Wark DA, Williams CA, Watson EB, Price JD (2003) Reassessment of pore shapes in microstructurally equilibrated rocks, with implications for permeability of the upper mantle. J Geophys Res 108(B1):2050, doi:10.1029/2001JB001575

Warren R (1968) Microstructural development during the liquid-phase sintering of two-phase alloys, with special reference to the NbC/Co system. J Mater Sci 3:471–85

Watson EB (1999) Lithologic partitioning of fluids and melts. Am Mineral 84:1693–1710

Watson EB, Brenan JM (1987) Fluids in the lithosphere, 1. Experimentally-determined wetting characteristics of CO_2–H_2O fluids and their implications for fluid transport, host-rock physical properties, and fluid inclusion formation. Earth Planet Sci Lett 85:497–515

Watson EB, Lupulescu A (1993) Aqueous fluid connectivity and chemical transport in clinopyroxene-rich rocks. Earth Planet Sci Lett 117:279–294

Yoshino T, Takei Y, Wark DA, Watson EB (2005) Grain boundary wetness of texturally equilibrated rocks, with implications for seismic properties of upper mantle. J Geophys Res 110:B08025, doi:10.1029/2004JB003544